

# 1 GEMS ozone profile retrieval: impact and validation of version 2 3.0 improvements

3 Juseon Bak<sup>1</sup>, Arno Keppens<sup>2</sup>, Daesung Choi<sup>3</sup>, Sungjae Hong<sup>3</sup>, Jae-Hwan Kim<sup>3</sup>, Cheol-Hee Kim<sup>3</sup>, Hyo-  
4 Jung Lee<sup>3</sup>, Wonbae Jeon<sup>3</sup>, Jhoon Kim<sup>4</sup>, Ja-Ho Koo<sup>4</sup>, Joowan Kim<sup>5</sup>, Kanghyun Baek<sup>6</sup>, Kai Yang<sup>7</sup>, Xiong  
5 Liu<sup>8</sup>, Gonzalo G. Abad<sup>8</sup>, Klaus-Peter Heue<sup>9</sup>, Jean-Christopher Lambert<sup>2</sup>, Yeonjin Jung<sup>10</sup>, Hyunkee  
6 Hong<sup>11</sup>, Won-Jin Lee<sup>11</sup>

7 <sup>1</sup>Institute of Environmental Studies, Pusan National University, Busan 46241, Republic of Korea

8 <sup>2</sup>Royal Belgian Institute for Space Aeronomy (BIRA-IASB), Brussels, Belgium

9 <sup>3</sup>Department of Atmospheric Sciences, Pusan National University, Busan 46241, South Korea

10 <sup>4</sup>Department of Atmospheric Sciences, Yonsei University, Seoul, Republic of Korea

11 <sup>5</sup>Department of Atmospheric Sciences, Kongju National University, Kongju, Republic of Korea

12 <sup>6</sup>NASA Goddard Space Flight Center, Greenbelt, Maryland, USA

13 <sup>7</sup>Department of Atmospheric and Oceanic Science, University of Maryland, College Park, MD 20742, USA

14 <sup>8</sup>Smithsonian Astrophysical Observatory (SAO), Center for Astrophysics | Harvard & Smithsonian, Cambridge, MA 02138,  
15 USA

16 <sup>9</sup>Institut für Methodik der Fernerkundung am Deutschen Zentrum für Luft- und Raumfahrt (DLR), Oberpfaffenhofen, Germany

17 <sup>10</sup>Major of Spatial Information Engineering, Division of Earth and Environmental System Sciences, Pukyong National  
18 University, Busan, Republic of Korea

19 <sup>11</sup>National Institute of Environmental Research, Incheon 22689, Republic of Korea

20

21 *Correspondence to:* Juseon Bak ([juseonbak@pusan.ac.kr](mailto:juseonbak@pusan.ac.kr)), Jaehwan Kim ([jaekim@pusan.ac.kr](mailto:jaekim@pusan.ac.kr))

22 **Abstract.** This study presents the first comprehensive description of the operational GEMS (Geostationary Environment  
23 Monitoring Spectrometer) ozone profile retrieval algorithm and evaluates the performance of the reprocessed version 3.0  
24 dataset. The retrieval operates in the 310–330 nm spectral range and yields total degrees of freedom for ozone ranging from  
25 1.5 to 3. Although the vertical sensitivity is limited, GEMS achieves an effective vertical resolution of 5–10 km and is capable  
26 of separating tropospheric and stratospheric ozone layers. This work highlights significant algorithmic and calibration  
27 improvements in version 3.0. Radiometric offsets in irradiance measurements are corrected using a scaling factor derived from  
28 the average ratio to a solar reference, while residual wavelength-dependent biases in the normalized radiance are further  
29 mitigated through soft calibration. In addition, shift corrections are applied separately to irradiance and radiance wavelengths.  
30 As a result, version 3.0 significantly reduces spectral fitting residuals, lowering them from 0.8% in version 2.0 to 0.2% under  
31 nominal conditions. This improvement also mitigates altitude-dependent oscillating biases observed in the previous version  
32 (+40 DU in the troposphere, -20 DU in the stratosphere). The version 3 ozone profiles show agreements within  $\pm 10$  DU of  
33 ozonesonde observations, with a mean bias of -7.7% in tropospheric ozone columns and within 5% in the stratosphere.  
34 Furthermore, the retrievals capture day-to-day vertical ozone variability, as demonstrated by comparisons with daily  
35 ozonesonde launches in February and March 2024. Integrated ozone columns derived from the profiles also show improved

36 consistency with ground-based total ozone measurements, yielding a mean bias of  $-3.6$  DU and outperforming the GEMS  
37 operational total column ozone product.

39 **1 Introduction**

41 Atmospheric ozone is a powerful greenhouse gas and air pollutant, harming human health and ecosystems in the  
42 troposphere (Van Dingenen et al., 2009; Isaksen et al., 2009). In the stratosphere, ozone is essential for protecting life on Earth  
43 by absorbing harmful ultraviolet (UV) radiation from the Sun (Solomon, 1999). It also plays a key role in maintaining the  
44 Earth's radiative balance and stratospheric temperature structure (Monks et al., 2015). Monitoring both layers is vital for  
45 understanding pollutant transport, regulating air quality, addressing climate change, and protecting environmental health.

46 The Geostationary Environmental Monitoring Spectrometer (GEMS) onboard the Korean GEO-  
47 KOMPSAT(Geostationary Korea Multi-Purpose Satellite)-2B satellite provides high temporal and spatial resolution data on  
48 ozone, its precursors ( $\text{NO}_2$  and  $\text{HCHO}$ ),  $\text{SO}_2$ , and aerosols over East Asia (Kim et al., 2020). GEMS offers two primary ozone  
49 products: total column ozone ( $\text{O}_3\text{T}$ ) and the full ozone profile ( $\text{O}_3\text{P}$ ). The  $\text{O}_3\text{T}$  product is retrieved using the historical TOMS  
50 look-up table algorithm (Kim et al., 2024), while the  $\text{O}_3\text{P}$  product provides vertically resolved ozone information across 24  
51 atmospheric layers, retrieved based on an optimal estimation-based inversion framework (Bak et al., 2020). A comprehensive  
52 evaluation of GEMS v2.0  $\text{O}_3\text{T}$  product has been conducted by Baek et al. (2023;2024), assessing its spatial and temporal  
53 representativeness on hourly, daily, and seasonal scales through cross-comparisons with ground-based Pandora measurements  
54 and independent satellite observations from polar-orbiting platforms. The product revealed strong correlations with Pandora  
55 (0.97) and satellite data (0.99), but showed a pronounced seasonal and latitudinal dependence in mean bias, attributed to the  
56 absence of a calibration component accounting for the bidirectional transmittance distribution function (BTDF) in irradiance  
57 measurements (Kang et al., 2024). A minor update to the look-up table was subsequently implemented, resulting in the release  
58 of version 2.1 (Kim et al., 2024). Although the GEMS  $\text{O}_3\text{P}$  product has not yet been fully described in peer-reviewed literature,  
59 the algorithm implemented for processing version 2.0 closely follows the Smithsonian Astrophysical Observatory (SAO)  
60 ozone profile algorithm used for generating the Ozone Monitoring Instrument (OMI) Collection 3 ozone profile research  
61 product (Liu et al., 2010). The OMI ozone profile product has demonstrated its reliability in supporting studies of ozone  
62 variability driven by the chemical and dynamical processes, quantifying global tropospheric budget of ozone, and evaluating  
63 model representation (Bak et al., 2022; Hayashida et al., 2015; Kuang et al., 2017; Lu et al., 2018). However, the project  
64 *Product Evaluation of GEMS L2 via Assessment with S5P and Other Sensors (PEGASOS, funded by the European Space  
65 Agency)* reported the need for improvements prior to scientific use, citing significant altitude-dependent oscillating biases in  
66 the GEMS  $\text{O}_3\text{P}$  version 2.0 product, with deviations of up to 30 % in the troposphere and from  $-10$  % to  $-20$  % in the stratosphere  
67 (<https://www.dlr.de/en/eoc/research-transfer/projects-missions/pegasos>). In addition, the PEGASOS report identified large  
68 discrepancies between the GEMS  $\text{O}_3\text{P}$  and  $\text{O}_3\text{T}$  products. The inconsistencies in ozone profile quality between GEMS and

69 OMI can be attributed to differences in radiometric and wavelength calibration stability, rather than to the retrieval algorithm  
70 itself, which shares similar forward and inverse processes.

71 These findings motivated the development of version 3.0 of the GEMS ozone profile product, which incorporates  
72 improvements in spectral and radiometric calibration, including:

- 73 (1) on-orbit derivation of slit functions,
- 74 (2) wavelength calibration of both radiance and irradiance spectra,
- 75 (3) irradiance offset correction to address solar diffuser–induced angular dependence and long-term optical degradation,  
76 and
- 77 (4) soft calibration to correct residual radiometric biases in the normalized radiances.

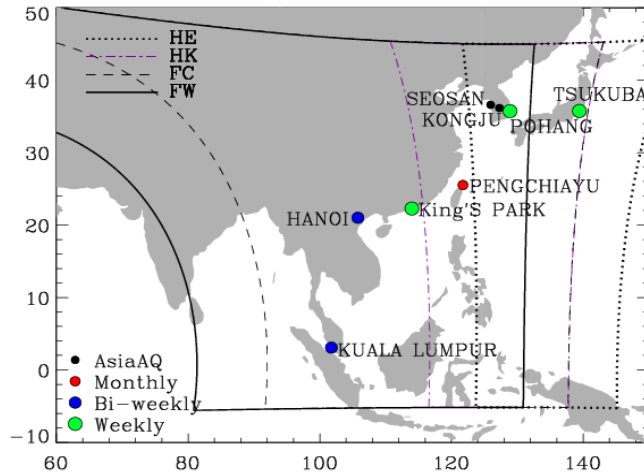
78  
79 In addition to these calibration enhancements, the algorithmic updates include modifications to the forward model  
80 calculations, fitting parameters, and several auxiliary inputs. This paper is structured around three main objectives. The  
81 retrieval algorithm and the updates from version 2.0 to version 3.0 are introduced in the second section. Section 3 focuses on  
82 retrieval characterization and error analysis based on optimal estimation diagnostics. Validation results using independent  
83 reference datasets are discussed in Section 4. The final section concludes this paper, with remarks for future updates.

## 84 85 **2. GEMS Ozone Profile Retrieval Algorithm**

### 86 **2.1 GEMS operations**

87 GEMS is an ultraviolet-visible imaging spectrograph equipped with a single two-dimensional charge-coupled device (CCD)  
88 array detector, with one dimension for 1,033 wavelengths and the other for 2,048 spatial pixels (Lee et al., 2024). It measures  
89 solar irradiance once each night and Earth’s backscattered radiance hourly from 07:45 to 16:45 Korea Standard Time (KST),  
90 covering the spectral range from 300 to 500 nm with a spectral resolution of approximately 0.6 nm full width at half maximum  
91 (FWHM). A shared optical path is used for both radiance and irradiance measurements, except for dedicated solar diffusers,  
92 which operate on different duty cycles (daily and monthly) to manage sunlight intensity and prevent detector saturation. In  
93 GEMS, spatial pixels represent fixed ground-based observation points on Earth, aligned in the north–south direction, as viewed  
94 from geostationary orbit, covering latitudes from 5°S to 45°N. These spatial pixels correspond to the "cross-track pixels" in  
95 polar-orbiting satellites, which are aligned across the flight path. For Earth observation, GEMS scans an east–west swath from  
96 75°E to 145°E in approximately 700 mirror steps (scan lines) in full-scan mode and 350 mirror steps in half-scan mode. Four  
97 scan modes — Half East (HE), Half Korea (HK), Full Central (FC), and Full West (FW) — are operated sequentially, with  
98 their spatial extents shown in Figure 1 and the detailed schedule summarized in Supplementary Tables 1 and 2. Currently,  
99 Version 2 irradiance and Version 1.2.4 radiance products are used as the standard Level 1C inputs for subsequent Level 2

100 processing. Neither product has been reprocessed since the initial on-orbit testing, and the official data period began on  
101 November 1, 2020. To enhance computational efficiency and improve the signal-to-noise ratio, Level 1C and selected Level  
102 2 products (e.g., cloud, surface reflectance, total ozone) are also available with spatial binning at  $2 \times 2$  or  $4 \times 4$  pixels. The ozone  
103 profile retrieval specifically utilizes  $4 \times 4$  binned data, resulting in a  $512 \times 175$  frame dataset.



104  
105 **Figure 1. Geographic coverage of the four GEMS scan modes: Half East (HE), Half Korea (HK),**  
106 **Full Central (FC), and Full West (FW), indicated by the curved boundaries. Colored dots indicate ozonesonde stations with regular**  
107 **launches within the GEMS domain, classified by launch frequency: red for monthly, blue for bi-weekly, and green for**  
108 **weekly. Black dots represent additional sites that participated during the Asia-AQ campaign.**

## 110 2.2 Algorithm Heritage

111 The heritage of the ozone profile retrieval algorithm is rooted in long-standing efforts to develop, improve, and validate  
112 ozone profile retrievals from spaceborne instruments such as the Global Ozone Monitoring Experiment (GOME), the OMI,  
113 the Ozone Mapping and Profiler Suite (OMPS), and the Tropospheric Monitoring Instrument (TROPOMI) (Bak et al., 2017,  
114 2024, 2025a; Cai et al., 2012; Dobber et al., 2008; Liu et al., 2005, 2010; Zhao et al., 2021). The Optimal estimation technique  
115 (Rodgers, 2000) provides the theoretical foundation for solving the inverse problem, enabling the transformation of spectral  
116 measurements into geophysical quantities. The retrieval process iteratively adjusts the atmospheric state vector to minimize a  
117 cost function that accounts for both the mismatch between simulated and measured spectra and the deviation from the a priori  
118 constraints. This optimization critically depends on stable wavelength and radiometric calibration, as well as an accurate  
119 radiative transfer model, to ensure robust spectral fitting and reliable results. Algorithmic updates from the OMI Version 2.0  
120 research product by Bak et al. (2024) were incorporated into the development of the GEMS Version 3.0 ozone profile product.  
121 In addition, new calibration methodologies were implemented for GEMS L1C radiance and irradiance to ensure spectral fitting

122 stability and improve retrieval accuracy. The following sections provide a detailed description of the inversion framework and  
123 its implementation.

124 **2.3 Optimal Estimation**

125 The Optimal Estimation-based inversion (Rodgers, 2000) is physically regularized toward minimizing the difference  
126 between a measured spectrum  $\mathbf{Y}$  and a spectrum that is simulated by the forward model  $\mathbf{F}(\mathbf{X})$ . Given an atmospheric state  $\mathbf{X}$ ,  
127 the inversion is constrained by the measurement error covariance matrix  $\mathbf{S}_y$  and statistically regularized by an a priori state  
128 vector  $\mathbf{X}_a$  with a priori covariance matrix  $\mathbf{S}_a$ . The cost function (chi-square) and the updated equation for the posterior state  
129 vector  $\mathbf{X}$  at iteration step  $i + 1$  are written as

130 
$$\chi^2 = \|\mathbf{S}_y^{-\frac{1}{2}}\{\mathbf{K}_i(\mathbf{X}_{i+1} - \mathbf{X}_i) - [\mathbf{Y} - \mathbf{F}(\mathbf{X}_i)]\}\|_2^2 + \|\mathbf{S}_a^{-\frac{1}{2}}(\mathbf{X}_{i+1} - \mathbf{X}_a)\|_2^2 \quad (1) \text{ and}$$

131 
$$\mathbf{X}_{i+1} = \mathbf{X}_i + (\mathbf{K}_i^T \mathbf{S}_y^{-1} \mathbf{K}_i + \mathbf{S}_a^{-1})^{-1} [\mathbf{K}_i^T \mathbf{S}_y^{-1} (\mathbf{Y} - \mathbf{F}(\mathbf{X}_i)) - \mathbf{S}_a^{-1}(\mathbf{X}_i - \mathbf{X}_a)] \quad (2)$$

132 , where each component of the matrix  $\mathbf{K}$  is the derivative of the forward model to the actual atmospheric state, called the  
133 Jacobians or weighting function matrix.  
134

135 The posterior error covariance matrix, quantifying the total uncertainty in the retrieved state  $\hat{\mathbf{x}}$ , is given by:

136 
$$\hat{\mathbf{S}} = (\mathbf{K}^T \mathbf{S}_y^{-1} \mathbf{K} + \mathbf{S}_a^{-1})^{-1}. \quad (3)$$

138 The retrieval gain matrix  $\mathbf{G}$ , representing the sensitivity of the retrieval to the measurements, can be written as:

139 
$$\mathbf{G} = \hat{\mathbf{S}} \mathbf{K}^T \mathbf{S}_y^{-1} \quad (\mathbf{G} = \frac{\partial \hat{\mathbf{x}}}{\partial \mathbf{y}}). \quad (4)$$

140 The product of  $\mathbf{G}$  and  $\mathbf{K}$  then yields the averaging kernel matrix  $\mathbf{A}$ , which characterizes the sensitivity of the retrieved state to  
141 the true atmospheric state:

142 
$$\mathbf{A} = \mathbf{GK} \quad (\mathbf{A} = \frac{\partial \hat{\mathbf{x}}}{\partial \mathbf{x}_{true}}). \quad (5)$$

143 Beyond information content analysis, the matrices  $\mathbf{G}$  and  $\mathbf{A}$  also govern the retrieval error characteristics. Accordingly,  $\hat{\mathbf{x}}$  can  
144 be expressed as:

145 
$$\hat{\mathbf{x}} = \mathbf{A} \mathbf{x}_{true} + (\mathbf{I}_n - \mathbf{A}) \mathbf{x}_a + \mathbf{G} \sigma_y \quad (6)$$

146 , which represents a weighted combination of the true atmospheric state and a priori information, and adds the measurement  
147 noise. The retrieval uncertainty due to measurement noise is quantified by propagating  $\sigma_y$  from the measurement space into  
148 the state space through the gain matrix  $\mathbf{G}$ , resulting into the measurement error covariance matrix:

149  $\mathbf{S}_n = \mathbf{G}\mathbf{S}_y\mathbf{G}^T. (7)$

150 Meanwhile, the smoothing error covariance matrix, representing the retrieval uncertainty caused by limited vertical  
151 information, is defined as:

152  $\mathbf{S}_s = (\mathbf{A} - \mathbf{I})\mathbf{S}_a(\mathbf{A} - \mathbf{I})^T (8)$

153 These two contributions then add up to the total covariance as given in Eq. (3), or  $\hat{\mathbf{S}} = (\mathbf{I} - \mathbf{A})\mathbf{S}_a$ .

154 **2.4 Implementation details and algorithm updates**

155 The state vector  $\mathbf{X}$  includes 24 partial ozone columns, surface albedo (0<sup>th</sup> and 1<sup>st</sup> order wavelength terms), cloud fraction,  
156 and six additional calibration parameters (see Supplementary Table 3). The measurement vector  $\mathbf{Y}$  consists of the logarithms  
157 of the sun-normalized radiance spectra, which enhances retrieval stability by reducing the sensitivity to absolute radiance errors  
158 and Fraunhofer lines. Measurement errors ( $\sigma_y$ ) are assumed to be mutually uncorrelated. Since the GEMS L1C product does  
159 not provide measurement error estimates, a constant relative error of 0.2% is uniformly applied across the spectral range.  
160 Accordingly, the measurement error covariance matrix is defined as:

161  $\mathbf{S}_y = \text{diag}(\sigma_{y,1}^2, \sigma_{y,2}^2, \dots, \sigma_{y,n}^2).$

162 Correlations between ozone layers are accounted for in the a priori error covariance matrix using a correlation length  $L$  of 6  
163 km, defined as:

164  $\mathbf{S}_a = \sigma_i^a \sigma_j^a \exp(-(|i - j|/L)^2),$

165 where  $\sigma_i^a$  and  $\sigma_j^a$  are the a priori errors of the  $i^{\text{th}}$  and  $j^{\text{th}}$  components of the state vector, respectively. The updates from GEMS  
166 v2.0 to v3.0 mirror those from OMI v1.0 to v2.0. In particular, the radiative transfer model is replaced with the PCA-VLIDORT  
167 v2.6 (Bak et al., 2021) to enhance the simulation efficiency. A look-up table correction was also implemented to account for  
168 approximations in the radiative transfer calculation related to the number of streams, coarse vertical layering, and polarization  
169 treatment. The TSIS-1 Hybrid Solar Reference Spectrum (Coddington et al., 2021) is now used instead of the solar reference  
170 from Chance and Kurucz ( 2010). The ozone cross-section has been switched from BDM 1995 (Brion et al., 1993; Daumont  
171 et al., 1992; Malicet et al., 1995) to BW 2018 (Birk and Wagner, 2018). Notably, the a priori ozone profile, based on the  
172 tropopause-based ozone climatology (Bak et al., 2013), has been consistently used in GEMS v2.0, GEMS v3.0, and OMI v2.0.  
173 The temperature data are necessary to account for the temperature dependence of the ozone cross-section, while surface and  
174 tropopause pressures are used to define the 25-level pressure grids (Supplementary Fig. 1). The tropopause pressure is also  
175 used to convert the a priori ozone profile from a tropopause-based to a surface-based vertical coordinate system. For  
176 meteorological inputs, the Global Forecast System (GFS) of a National Centers for Environmental Prediction (NCEP) weather  
177 forecast model is used in the daytime processing (DRPO) mode. GFS data are downloaded daily at 05:00 KST, covering  
178 forecast periods between 6 KST and 18 KST, with lead times of 12 to 21 hours. In the reprocessing (RPRO) mode, the  
179 meteorological input is switched to the NCEP FNL (Final) Operational Global Analysis data. The meteorological fields,

180 provided at 3-hour intervals (GFS) or 6-hour intervals (FNL) per day, are interpolated to match the GEMS reference time.

181 **2.5 Calibration methodologies**

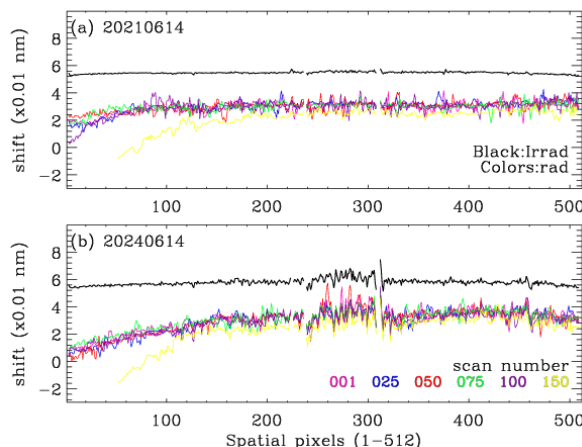
182 The calibration process consists of several key components: on-orbit slit function derivation and wavelength calibration  
183 to ensure spectral accuracy (Section 2.5.1), as well as irradiance offset correction and soft calibration to reduce radiometric  
184 uncertainties (Section 2.5.2).

185

186 **2.5.1 Spectral correction**

187 The instrument spectral response function (ISRF), or slit function is required to degrade high-resolution spectra (e.g.,  
188 absorption cross-sections) to match the spectral resolution of GEMS. Pre-flight ISRFs, measured at six discrete wavelengths  
189 and interpolated across all 1,322 wavelength grids, are available (Kang et al., 2022). However, our companion study proposes  
190 an on-orbit slit function derivation for GEMS based on a super-Gaussian model to account for temporal variations in the  
191 instrument response (Bak et al. 2025b), and is therefore not repeated here. That study also indicated that the irradiance spectrum  
192 should be shifted by 0.055 nm to align with the Fraunhofer lines. In most GEMS Level 2 trace gas algorithms, the irradiance-  
193 derived shift is applied directly to the radiance spectra, under the assumption that the spectral shifts for radiance and irradiance  
194 are similar. To address the limitation of our calibration approach, we have revised the manuscript. Therefore, independent shift  
195 correction is implemented to radiance and irradiance. To ensure computational efficiency, the radiance shift is determined  
196 from the first mirror step and applied uniformly along the scan direction, based on the observation that spectral shifts in the  
197 radiance data remain relatively uniform across mirror steps.

198



199

200      **Figure 2. Shifts of irradiance and radiance relative to the solar reference from Coddington et al. (2021), shown as a**  
201      **function of spatial pixel number (1–512) for (a) June 14, 2021 and (b) June 14, 2024. Colored lines represent scan lines**  
202      **(mirror steps) plotted at 25-intervals, ranging from 1 to 150.**

203

## 204      2.5.2 Radiometric correction

205      The GEMS irradiance is spatially and seasonally biased due to a missing calibration component for the BTDF, which  
206      defines how light transmits through a diffuser based on incident and outgoing angles—a well-known issue (Kang et al. 2024;  
207      Bak et al. 2025b). Additionally, Bak et al. (2025b) identified progressive radiometric degradation, resulting in an annual  
208      irradiance decrease of ~5% in the shorter UV range. They also reported that the measured irradiance is roughly 40% lower  
209      than the solar reference near 325 nm. Because normalized radiance is used in spectral fitting, such irradiance biases can directly  
210      propagate into retrieval output. To address these discrepancies, a major revision was implemented in version 3. Specifically, a  
211      correction factor was introduced to compensate for the systematic difference between the GEMS irradiance ( $I_m$ ) and a high-  
212      resolution solar reference spectrum ( $I_{ref}$ ). This correction factor (C) is derived by minimizing the following cost function:

213      
$$\chi^2 = \sum_{\lambda} (I_m(\lambda) - [C \cdot I_{ref}(\lambda + \Delta \lambda) \otimes S + \sum_m^3 P_b^m (\lambda - \bar{\lambda})^m])^2 \quad (9)$$

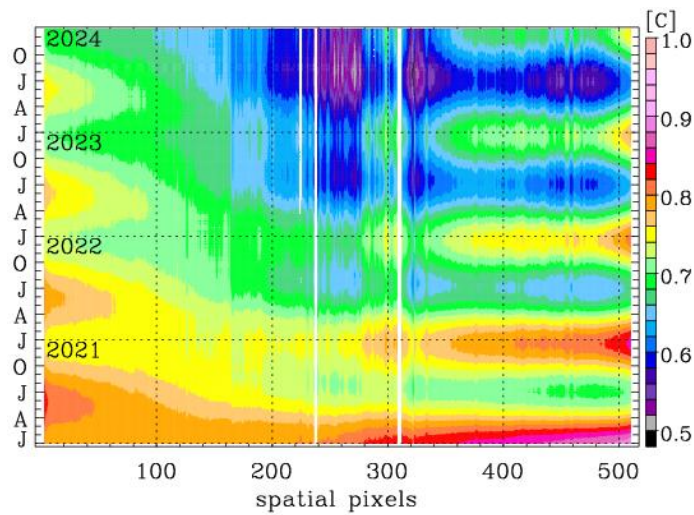
214      where:

- 215            • S: instrument spectral response function (ISRF)  
216            •  $\otimes$ : convolution operator,  
217            •  $\Delta \lambda$ : wavelength shift  
218            •  $P_b^m$ : coefficients of a third-order baseline polynomial centered at  $\bar{\lambda}$

219

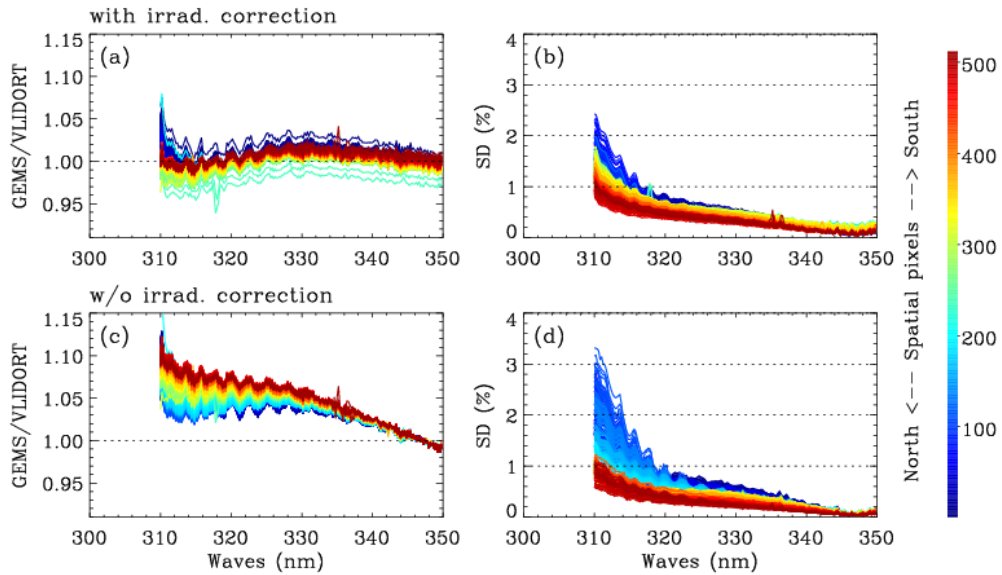
220      In this approach, the slit function parameters and the wavelength shift are first determined independently and then held fixed,  
221      allowing the solar reference spectrum to be adjusted to the measured irradiance in terms of spectral resolution and spectral  
222      alignment. The scaling factor  $C$  and the baseline polynomial  $P_b$  are subsequently fitted to capture remaining radiometric  
223      differences. As presented in Figure 3, the derived values of  $C$  exhibit significant seasonal and spatial variations in irradiance  
224      offset related to angular dependence, along with a gradual temporal decline attributable to optical degradation, most  
225      prominently at the middle spatial pixels. In version 3, only the scaling factor  $C$  is applied in the irradiance correction, by  
226      dividing the irradiance by  $C$ . This decision was made because applying the baseline polynomial  $P_b$  directly to the irradiance  
227      introduced artificial structures into the spectral fitting of the normalized radiance, resulting in a significant underestimation of  
228      stratospheric ozone retrievals. Residual wavelength-dependent uncertainties are instead addressed through the soft calibration

229 process, which has been newly implemented in version 3. This empirical correction eliminates systematic biases in the  
230 normalized radiance by applying adjustment factors derived from the ratio of measurements to simulated spectra based on  
231 accurate forward model calculations. The ozone profile input for the forward model calculation is constructed using daily zonal  
232 mean Microwave Limb Sounder (MLS) data (Livesey et al., 2025) above 215 hPa and climatological profiles (McPeters and  
233 Labow, 2012) below that level, with the integrated total column adjusted to match the zonal mean total ozone from daily  
234 OMPS measurements (Jaross, 2017). A one-week set of clear sky measurements, collected at 02:45 UTC between July 11 and  
235 17, 2021, is used to derive the soft calibration spectra as a function of the 512 spatial pixels. While a cloud fraction threshold  
236 of 0.2 is typically used to define clear-sky conditions, we relaxed this criterion to 0.4 due to the known overestimation in the  
237 GEMS cloud product, which is also affected by irradiance offsets. Figure 4 illustrates the derived soft spectra and the impact  
238 of applying the irradiance correction. After correction, the soft calibration spectra show significantly reduced biases and  
239 improved spatial consistency. The residual biases are generally positive and remain below 3% for most pixels, except for a  
240 few central pixels that exhibit negative values, possibly due to unflagged dead pixels in the GEMS L1C data. In contrast,  
241 without the correction, substantial wavelength-and spatially dependent biases are evident, with systematic biases ranging from  
242 3% to 10% in the shorter UV range. Moreover, the standard deviation of the residual spectra stays below 1% for spatial pixels  
243 numbered below 100, while it increases above 3% for pixels above 400 without correction. With correction applied, this  
244 increase is limited to 2 %. Figure 5 demonstrates the resulting improvement in spectral fitting accuracy achieved through the  
245 application of both radiometric (scaling correction to irradiance and soft calibration to normalized radiance) and wavelength  
246 calibration in version 3, compared to version 2. With these corrections, mean fitting residuals decreased from approximately  
247 0.8% in v2.0 to 0.2% in v3.0 across most spatial pixels, representing more than a fourfold enhancement in retrieval precision.  
248 Version 3.0 not only reduces the mean fitting residuals but also achieves substantial improvements in seasonal stability, spatial  
249 uniformity, and the removal of systematic and random artifacts, —highlighting the effectiveness of the enhanced calibration  
250 and retrieval procedures.



251

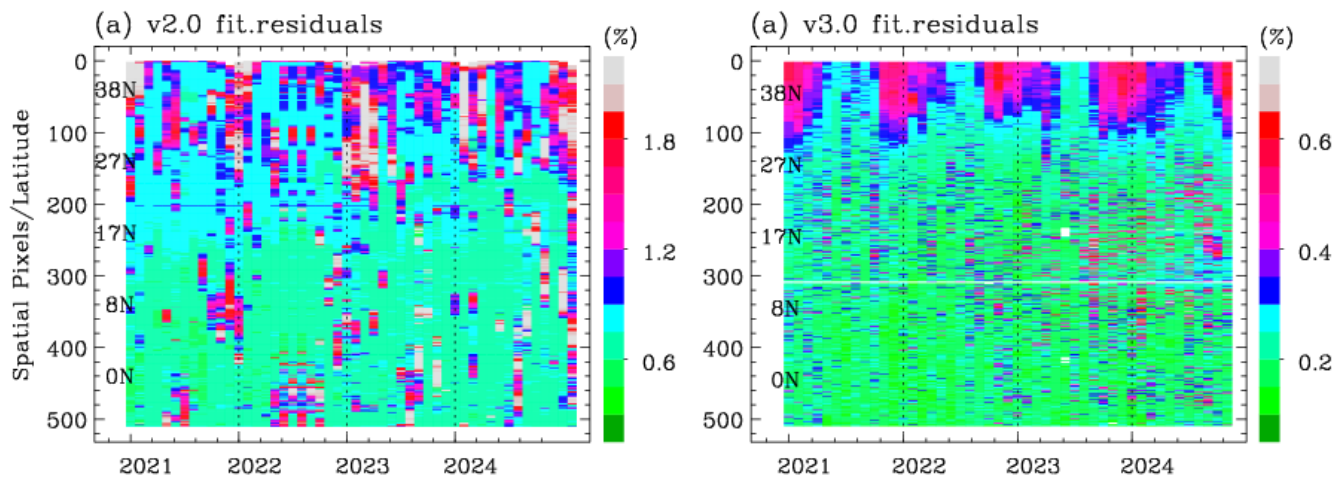
252 **Figure 3. Time–space distribution of the derived correction factor C across 512 spatial pixels from January 2021 to**  
 253 **December 2024. The factor C, fitted over the 310–330 nm spectral window, represents the ratio of GEMS irradiance to**  
 254 **a high-resolution solar reference spectrum.**



255

256 **Figure 4. GEMS soft spectrum, derived as the mean difference between measured and simulated normalized radiances,**  
 257 **as a function of wavelength (300–350 nm) for each of the 512 spatial pixels (color-coded from north to south), with the**  
 258 **standard deviation of the mean difference. The upper panel includes the scaling correction for the irradiance offset,**  
 259 **while the bottom panel does not.**

260



261  
 262 **Figure 5. Comparison of spectral fitting quality from ozone profile retrievals between versions 2.0 and 3.0, averaged**  
 263 **over the first 20 scanlines and shown as a function of the 512 spatial pixels. The evaluation is performed on the 15th**

264 day of each month from 2021 to 2024 (04:45 UTC). Fitting residuals, calculated as the root mean square (RMS) of the  
265 relative differences between measured and simulated radiance (%), are stored as “ResidualOffit” in version 2 and  
266 “avg\_residuals” in version 3. Note that the color scale range in panel (b) is narrowed to one-third of panel (a) to enhance  
267 the visibility of the lower residual values.  
268  
269

### 270 3. Retrieval Characterization

271

272 The averaging kernel matrix (AKM) and error covariance matrix (CVM) are used to characterize the retrieval sensitivity  
273 and its associated uncertainties. Their characteristics are mainly governed by the fitting window, measurement noise, and the  
274 a priori covariance matrix, and they remain largely unchanged between versions 2 and 3 of the retrieval algorithm. The rows  
275 of the AKM serve as vertical smoothing functions, representing the sensitivity of the retrieved ozone to changes in the true  
276 atmospheric state (see Eq. 5). The trace of the AKM, referred as the degrees of freedom for signal (DFS), quantifies the number  
277 of independent pieces of information available from the measurements. Retrieval uncertainty, given by the square root of the  
278 CVM diagonal, is assessed against the a priori uncertainty, considering both the total error and the contribution from  
279 measurement noise alone.

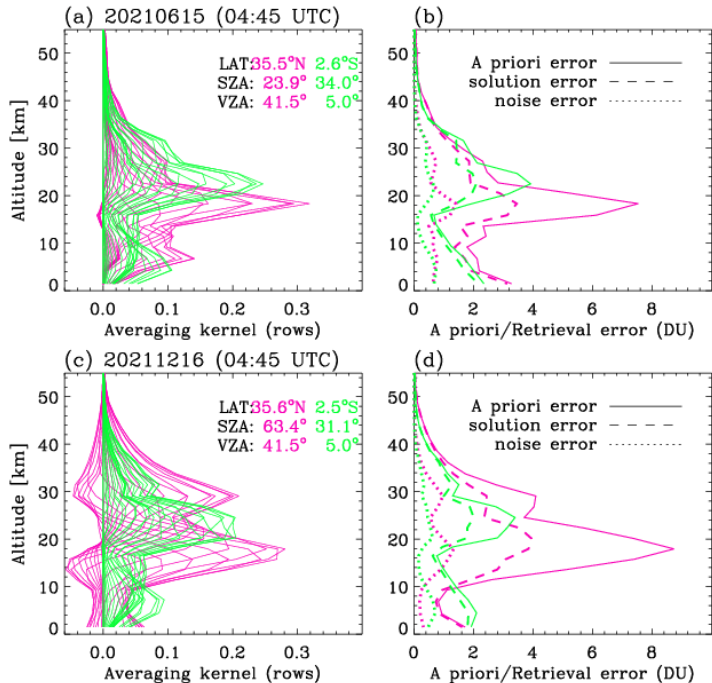
280 Figure 6 shows the mean averaging kernels and uncertainty profiles from the GEMS 04:45 UTC scans, covering two  
281 regions with different viewing zenith angles (VZA) and two dates with different solar zenith angles (SZA).  
282  
283  
284

285 The averaging kernels peak notably just below the stratospheric ozone layer and within the upper troposphere–lower  
286 stratosphere (UTLS), where the a priori uncertainty is largest, indicating that the retrieval provides the greatest information  
287 content. The vertical location of these peaks is strongly influenced by the optical path length (SZA and VZA). At the kernel  
288 peaks, the retrieval uncertainty is reduced by ~ 50 % with respect to the a priori, with about one-third of the total (solution)  
289 error being due to measurement noise. Away from the peaks, the reduction in uncertainty is generally smaller. At high SZAs,  
290 negative kernel oscillations are evident, reflecting challenges in vertically allocating the measurement information. This  
291 suggest that the retrieval may offer only limited improvement over the prior under such conditions.

292 Figure 7 presents the sub-column DFS values for the troposphere and stratosphere. The corresponding ozone partial  
293 columns are provided in Supplementary Fig. 2, reflecting the expected dependence of information content on atmospheric  
294 ozone concentration. The stratospheric DFS increases with optical path length, and thus with latitude (Fig. 7.c, d), whereas the  
295 tropospheric DFS shows the opposite behaviour, with higher values at lower SZA/VZA (Fig. 7a.b). This relationship becomes  
296 more complex by factors such as tropospheric ozone abundance, surface reflectance, and other scene-dependent characteristics  
297 including aerosol and clouds. In the summer case, the tropospheric DFS indicates that the retrieval yields more information

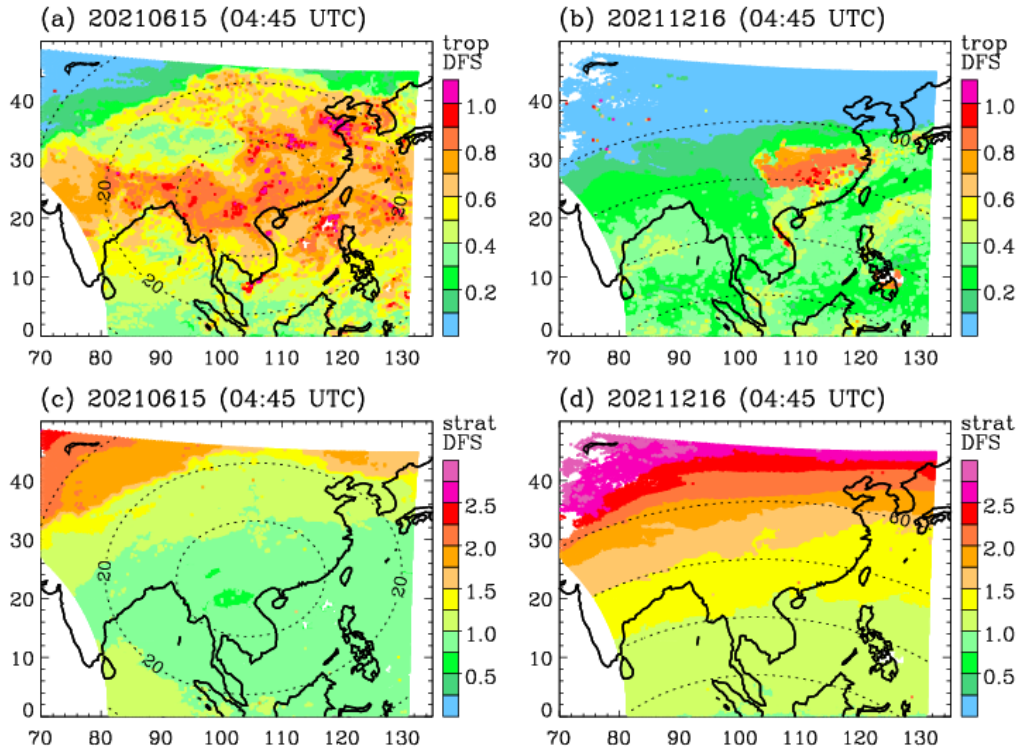
298 when ozone concentrations are higher, resulting in stronger absorption signals (0.5-1.0 DFS). In the December case,  
299 tropospheric DFS values generally range from 0.2 to 0.5 at latitudes below 30°. Abnormally high DFS values (0.7-0.9) are  
300 linked to elevated surface albedo, retrieved as a compensation for missing cloud information in pixels where the GEMS Level  
301 2 cloud product fails to provide valid output (Supplementary Fig. 3). Summing the tropospheric and stratospheric contributions,  
302 the total DFS ranges from 1.5 to 3, with a compensating effect observed at higher latitudes, where decreases in tropospheric  
303 DFS are offset by increases in stratospheric DFS.

304



305

306 **Figure 6. Averaging kernels and retrieval errors of ozone profiles from the 04:45 UTC scans on 15 June (a, b) and 16**  
307 **December (c, d) 2021. Pink and green lines indicate averages over cross-track pixels 50-100 and 450-550, respectively,**  
308 **at the first scan line.**



309  
310 **Figure 7. Degrees of freedom for signal (DFS) for tropospheric column ozone on (a) 15 June and (b) 16 December 2021,**

311 and analogous for the stratospheric column in (c) and (d), respectively. Contours indicate the solar zenith angle (SZA)

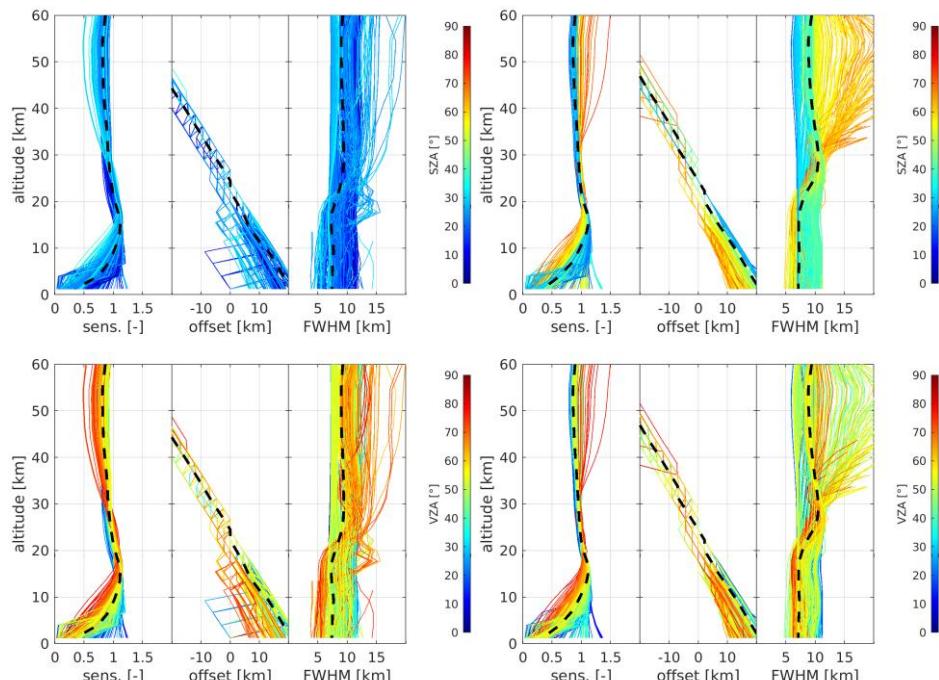
312 at 20° intervals. The corresponding ozone distributions are shown in Supplementary Figure 2.

313  
314 In this work, we further examine three supplementary diagnostics: the retrieval sensitivity, retrieval offset and effective  
315 vertical resolution (which differs from the sampling resolution), following Keppens et al. (2015). The sum of each row of the  
316 AKM quantifies the total retrieval sensitivity, providing a vertically resolved and normalized measure of the contribution from  
317 satellite observations relative to the a priori profile. The retrieval offset indicates any vertical mismatch between the location  
318 of maximum sensitivity (the retrieval barycenter) and the nominal retrieval altitude (Rodgers, 2000). The effective vertical  
319 resolution is defined by the FWHM of each averaging kernel. This measure, however, does not account for averaging kernel  
320 oscillations, including the occurrence of negative values (see Fig. 6). Figure 8 presents the retrieval diagnostics described  
321 above—sensitivity, offset, and vertical resolution—for GEMS ozone profile retrievals, evaluated from every tenth mirror step  
322 and spatial pixel, yielding on the order of 1000 profiles for the 04:45 UTC scan. The results show that, on average, the vertical  
323 sensitivity of the retrievals is close to unity throughout most of the profile. Sensitivity drops below 0.5 only in the lowest 5 km,  
324 with higher values occurring above highly reflective surfaces (e.g., high cloud fractions). In the troposphere, vertical sensitivity  
325 generally increases with shorter optical paths (e.g., lower SZA and VZA), which enhance atmospheric penetration. In the  
326 stratosphere, however, higher sensitivities occur under more oblique viewing geometries (higher VZA), particularly during

327 winter when large SZAs further enhance the DFS. By contrast, in summer, when SZAs are smaller, stratospheric sensitivity is  
328 lower for near-nadir viewing angles (i.e., shorter path lengths).

329 Outside the UTLS (about 15-30 km), the retrieval barycenter deviates nearly linearly from the nominal retrieval altitude.  
330 Consequently, the vertical sensitivity is primarily distributed off-diagonal, with its barycenter residing in the UTLS (as can  
331 also be seen from the averaging kernel peak positions in Figure 6). In the troposphere, the retrieval offset depends on SZA and  
332 VZA (and thus latitude), but shows no other significant dependences on the influence quantities examined (Supplementary  
333 Fig. 4). The offset decrease under more oblique solar and viewing geometry (larger SZA and VZA), although this is  
334 accompanied by a reduction in tropospheric retrieval sensitivity.

335 The average effective vertical resolution of the GEMS ozone profiles ranges from 6 to 10 km. Both in the troposphere  
336 and stratosphere, they strongly depend on SZA and VZA. However, opposite behaviors are observed above and below the  
337 tropopause: longer path lengths lead to coarser vertical resolution (larger FWHM) in the troposphere, while in the stratosphere,  
338 especially under very high SZA, they result in finer vertical resolution, with the retrieved information distributed over a larger  
339 vertical extent.



340  
341 **Figure 8: Sensitivity, offset, and kernel FWHM for GEMS ozone profile retrievals on June 15 (left) and December 16  
342 (right) 2021. Black dashed lines indicate median values. Color coding represents SZA (top) and VZA (bottom), which  
343 are the primary quantities influencing retrieval characteristics; additional factors are presented in the Supplement.**

344 **4. Validation using independent reference datasets**

345 As a preliminary step in establishing a reliable validation framework for GEMS ozone profile retrievals, Bak et al. (2019)  
 346 evaluated ozonesonde soundings from 10 East Asian sites and found that electrochemical concentration cell (ECC) sensors  
 347 provided more reliable measurements than modified Brewer–Mast (MBM) and carbon–iodine (CI) sondes. They also  
 348 emphasized the importance of maintaining consistent procedures across the preparation, operation, and post-processing stages  
 349 to ensure long-term data quality and consistency. Among these sites, five—Pohang, King’s Park, Tsukuba, Hanoi, and Kuala  
 350 Lumpur—have remained active during the GEMS mission, regularly launching balloon-borne ECC ozone sensors. Weekly  
 351 regular observations have continued at Pohang, King’s Park, and Tsukuba in the afternoon (1:30-2:30 pm LT). Hanoi and  
 352 Kuala Lumpur, where ozonesondes are launched bi-weekly, were not recommended as reference sites in Bak et al. (2019)  
 353 because of frequent changes in sensing solution concentrations or the ozonesonde manufacturer. During the GEMS operational  
 354 period, however, these inconsistencies have been better managed, and data from these sites are therefore included in this study.  
 355 In addition, monthly ozonesonde observations from Pengchiayu, initiated in 2022, are also incorporated. Table 1 summarizes  
 356 the availability of the regular ozonesonde sites used for GEMS validation in Section 4.1. In Section 4.2, we further include 13  
 357 ozonesondes launched at Seosan (126.38°E, 36.92°N) and 10 launched at Kongju (127.74°E, 36.47°N), South Korea, as part  
 358 of the 2024 Airborne and Satellite Investigation of Asian Air Quality campaign (NASA, 2023). Integrated total ozone columns  
 359 were also evaluated at Seosan during the ASIA-AQ campaign (Section 4.2) using Pandora measurements.

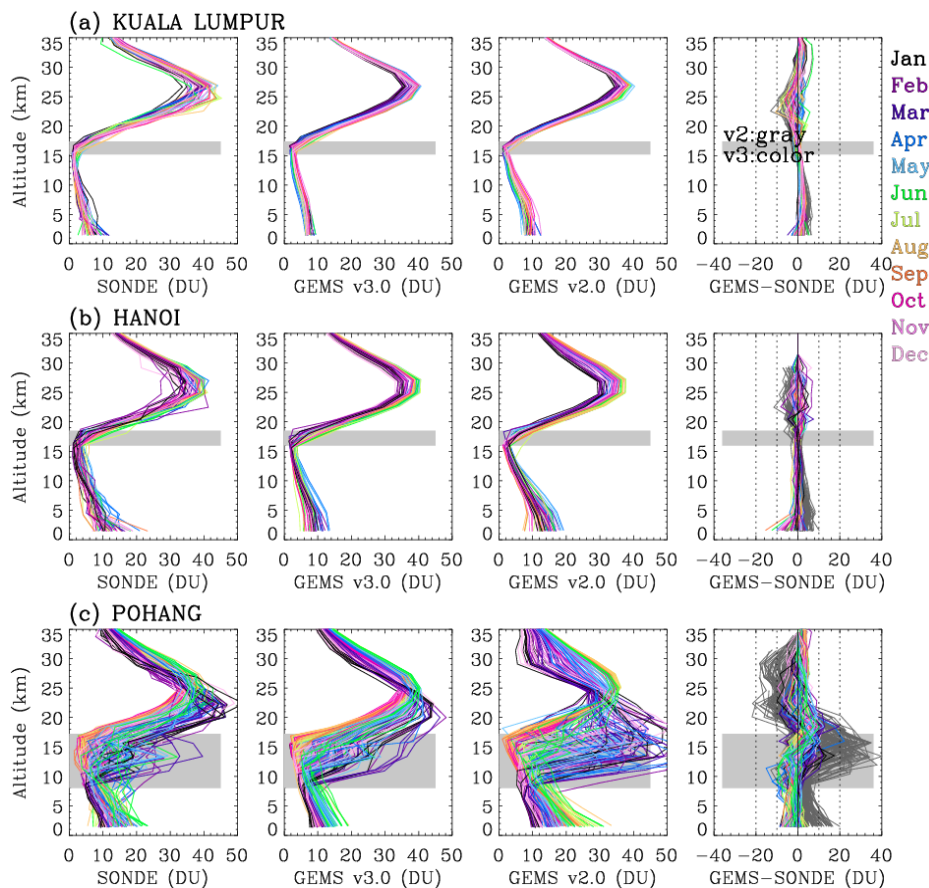
360  
 361 **Table 1. List of regular ozonesonde stations used in this study.**

Station	Pohang	Tsukuba	King’s park	Hanoi	Pengchiayu	Kuala Lumpur
Country	South Korea	Japan	Hong Kong	Vietnam	Taipei	Malaysia
Lon, Lon (deg.)	36.03, 129.38	36.06, 140.13	22.31, 114.17	21.02, 105.804	25.63, 122.08	2.73, 101.7
Provider <sup>#</sup>	KMA	WOUDC	WOUDC	SHADOZ	WOUDC	SHADOZ
Frequency	Weekly	Weekly	Weekly	Bi-weekly	Monthly	Bi-weekly
Launch Time (LT)	2:00 pm	2:30 pm	1:30 pm	1:00 pm	12:00 am	12: 30 am
Beginning date	1995-01-12	2017-06-22	2000-01-05	2004-09-18	2022-04-18	1998-05-04
Latest update	2024-06-26	2025-02-27	2024-12-31	2024-02-23	2024-05-12	2022-12-22

362 #KMA (Korea Meteorological Administration), WOUDC (World Ozone and Ultraviolet Radiation Data Centre), SHADOZ  
363 (Southern Hemisphere ADDitional OZonesondes)  
364  
365

366 **4.1 Validation with regular ozonesonde soundings**

367



368

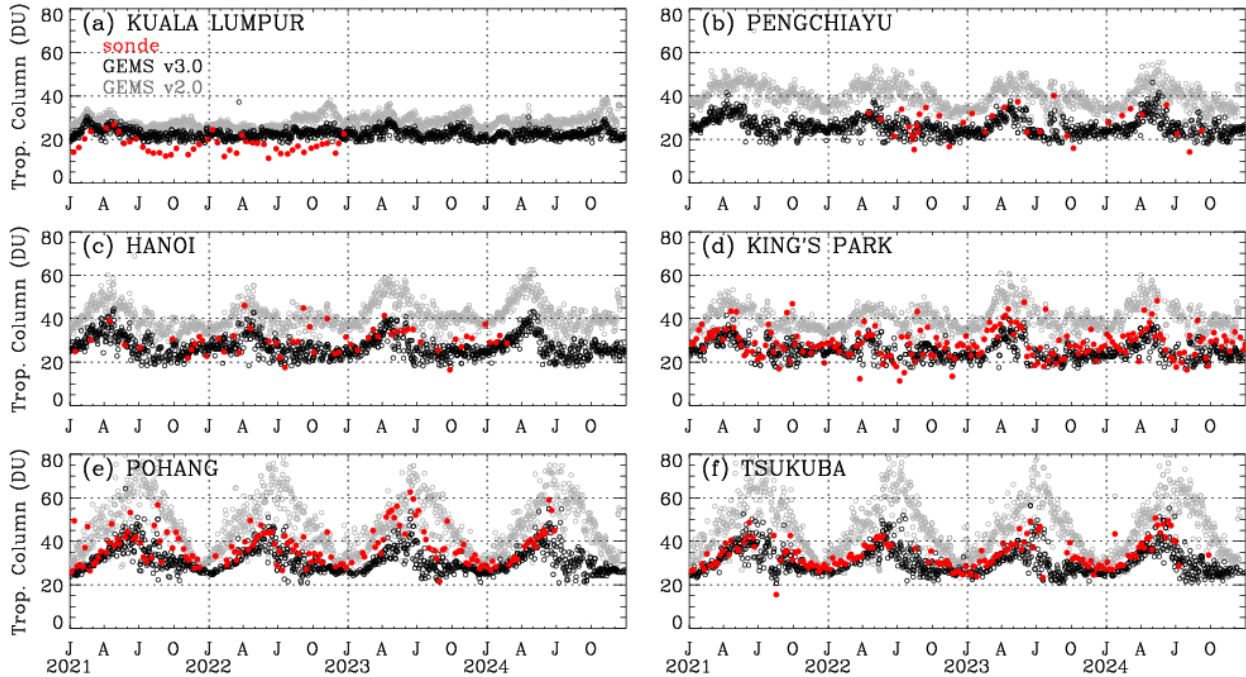
369 **Figure 9. Ozone vertical profiles (in DU) at three sites—(a) Kuala Lumpur, (b) Hanoi, and (c) Pohang—during 2021–  
370 2024. Each panel displays individual ozonesonde soundings along with corresponding GEMS v3.0 and v2.0 retrievals.  
371 The last columns present the respective differences (GEMS – SONDE) for GEMS v3.0 and v2.0, displayed in color and  
372 dark gray, respectively. The gray shaded area denotes the range of tropopause altitudes (minimum to maximum).**  
373

374

375 Ozonesondes are used to validate GEMS measurements from FW scans, which provide better temporal coincidence in the  
afternoon (Table 1; Supplementary Tables 1-2). However, those from Tsukuba are matched with GEMS FC scan measurements

376 due to spatial constraints (See Fig. 1). Figure 9 illustrates how well GEMS captures the vertical distribution of ozone up to 35  
 377 km—the typical burst altitude of ozonesonde balloons—at three stations representing different latitudinal bands: mid-latitudes  
 378 (Pohang), subtropics (Hanoi), and tropics (Kuala Lumpur). The latest GEMS version (v3.0) demonstrates substantial  
 379 improvements, particularly at the mid-latitude site of Pohang. Tropospheric ozone agrees within 10 DU of ozonesonde  
 380 measurements, while stratospheric ozone is within 5 DU. However, GEMS v2.0 exhibited high biases in tropospheric ozone  
 381 of up to 20 DU, reaching 40 DU near the tropopause, while underestimating stratospheric ozone columns by as much as 20  
 382 DU. At lower-latitude sites, both GEMS v2.0 and v3.0 produce qualitatively similar ozone profiles, as the vertical structure  
 383 shows relatively weak seasonal variability and the tropopause altitude remains stable, making the retrievals easier to constrain  
 384 with a priori information.

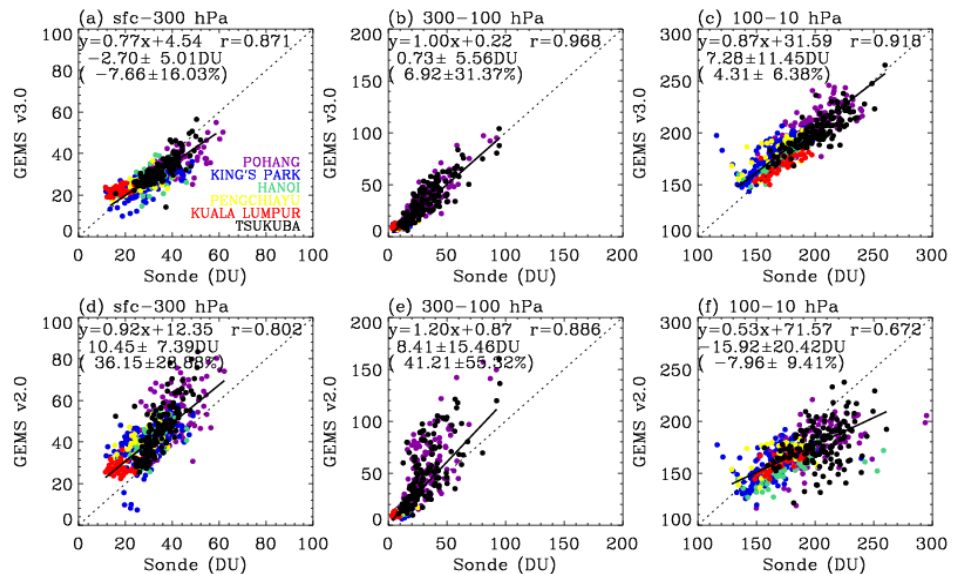
385 Figure 10 presents time series comparisons of lower tropospheric ozone columns (below 300 hPa) derived from GEMS  
 386 (v2.0 in gray and v3.0 in black) and ozonesonde observations (in red) at six stations across different latitudes during the period  
 387 2021 to 2024.



389  
 390 **Figure 10. Time-series of tropospheric ozone columns (surface-300 hPa) from GEMS v3.0 (black), GEMS v2.0 (grey),**  
 391 **and ozonesondes (red). The x-axis marks the months of the year using initials: J (January), A (April), J (July), and O**  
 392 **(October).**

393 Mid-latitude sites (Pohang and Tsukuba) exhibit pronounced seasonality, with ozonesonde-derived tropospheric ozone  
 394 columns ranging from 25 to 50 DU—peaking in summer and declining toward winter. Within the summer season, ozone levels

395 typically reach their maximum in June, followed by a sharp decline in July and August. As shown, GEMS v3.0 reasonably  
 396 reproduces this seasonal pattern. At subtropical sites such as Hanoi, King's Park, and Pengchiayu, seasonal changes are less  
 397 pronounced, with ozone columns typically fluctuating between 20 and 45 DU. A distinct spring peak of 40-45 DU is  
 398 consistently observed in both ozonesonde and GEMS v3.0 time-series. The lowest ozone levels are observed between July and  
 399 October, remaining a few DU lower than the wintertime minimum. At the tropical site of Kuala Lumpur, ozonesonde  
 400 measurements are limited in 2021 and 2022, but the available data suggest minimal seasonal variation in tropospheric ozone,  
 401 consistent with the weak seasonal signals typically observed in the tropics. With its dense temporal coverage, GEMS v3.0  
 402 complements the sparse ozonesonde measurements and identifies the flat tropospheric ozone levels throughout the 2021-2024  
 403 period. However, GEMS v2.0 systematically retrieves higher ozone levels across all latitudinal bands. This overestimation is  
 404 much more pronounced at mid-latitudes than at lower latitudes. In particular, GEMS v2.0 significantly overestimates summer  
 405 ozone values by 30 DU compared to GEMS v3.0, with the discrepancy decreasing toward winter. In the subtropics, the  
 406 difference between GEMS v2.0 and v3.0 remains about 15 DU, without clear seasonal change. In particular, GEMS v2.0  
 407 retrieves higher ozone amounts in 2023 and 2024 compared to earlier years, which is not reflected in either GEMS v3.0 or  
 408 ozonesonde data. This increasing discrepancy is likely associated with the optical degradation of the instrument, which leads  
 409 to decreasing irradiance values over time (Kang et al. 2024; Bak et al. 2025b) and, in turn, affects the accuracy of the ozone  
 410 profile retrievals. In the tropics, the GEMS products from both versions agree within 5 DU during 2021–2022, but the  
 411 difference increases to within 10 DU in 2023–2024. Notably, the issues identified in GEMS v2.0 are substantially mitigated  
 412 in GEMS v3.0, owing to the newly implemented radiometric calibration applied to both irradiance and normalized radiance.



413

414 **Figure 11.** Scatter plots of GEMS and ozonesonde ozone columns for three different layers, surface-300 hPa, 300-100  
 415 hPa, and 100-10 hPa. The upper (a-c) panels show results from GEMS v3.0, and the bottom panels (d-f) from GEMS

416 **v2.0. Each data pair is color-coded by station. Regression lines and correlation coefficients (r) are derived from all data**  
417 **pairs, along with the mean bias and standard deviation reported in both DU and percentage.**

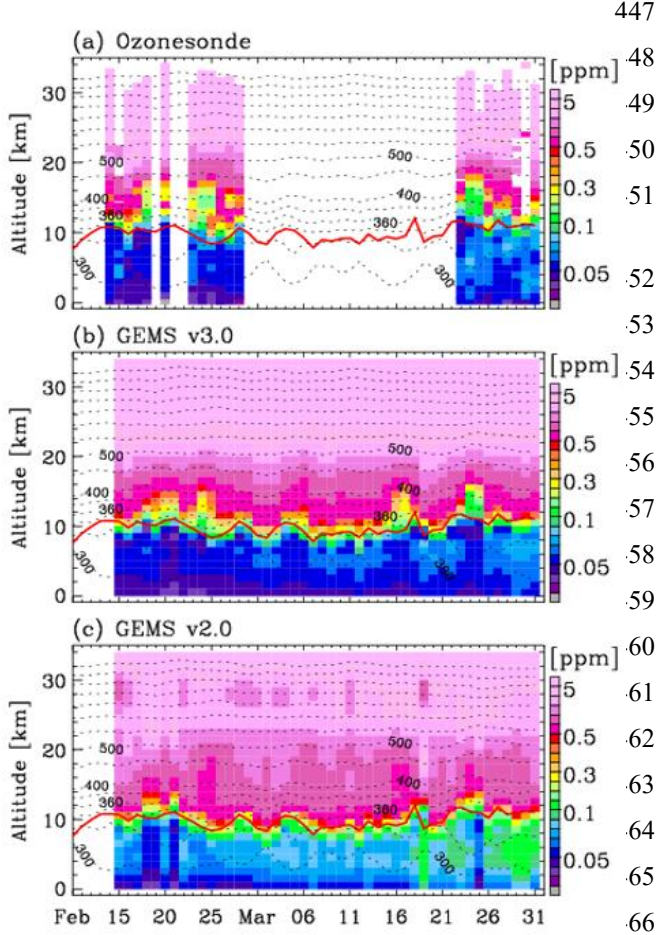
418

419 The quantitative comparison between GEMS and ozonesonde measurements is presented in Figure 11 (a, d) for  
420 tropospheric ozone columns below 300 hPa. Compared to version 2.0, which exhibits a substantial positive bias of 36.15%  
421 and high variability ( $\pm 28.88\%$ ), GEMS v3.0 shows a marked improvement, reducing the bias to  $-7.66\%$  with lower scatter  
422 ( $\pm 16.03\%$ ) and achieving a higher correlation with ozonesonde observations ( $r = 0.87$  vs.  $r = 0.80$ ). The regression slope for  
423 GEMS v2.0 is closer to unity than that of v3.0, due to the presence of both negative biases at high-ozone sites and positive  
424 biases at low-ozone sites, whereas v2.0 shows more uniform positive biases across stations. Figure 11 also evaluates ozone  
425 partial columns in upper troposphere and lower stratosphere (UTLS: 300-100 hPa) and the middle stratosphere (100-10 hPa),  
426 respectively. The 100–10 hPa layer, which corresponds to the ozone maximum in the upper stratosphere, also shows good  
427 agreement, with GEMS v3.0 achieving a correlation of  $r = 0.92$  and a relatively small mean bias ( $4.31 \pm 6.38 \%$ ), further  
428 supporting the reliability of the updated retrievals at higher altitudes.

429 The GEMS retrievals are inherently more influenced by a priori information compared to existing nadir satellite products  
430 such as OMI and TROPOMI, due to the narrower spectral range (310-330 nm versus 270-330 nm). Despite both versions  
431 employing the same a priori constraints, GEMS v2.0 exhibits poorer agreement with ozonesonde data than the a priori itself,  
432 reflecting the detrimental impact of radiometric uncertainties on the retrievals. However, GEMS v3.0 demonstrates better  
433 agreement than the a priori, indicating improved retrieval performance, especially when retrieving high ozone concentrations  
434 in both the troposphere and stratosphere. A comparison between GEMS a priori and ozonesondes is provided in Supplement  
435 Figure 4.

## 436 **4.2 Validation with Asia-AQ campaign ozonesonde soundings**

437 Figure 12a shows the date-altitude cross-section of ozone mixing ratios obtained from ozonesondes at Seosan (February)  
438 and Kongju (March) during the 2024 Asia-AQ campaign. As the two sites are only about 131 km apart, they are treated jointly  
439 in the analysis and considered to represent similar ozone seasonality. Ozone concentrations near the surface range from 30 to  
440 50 ppb, which are lower than those in the upper troposphere—approximately 60 ppb in February and increasing to 80 ppb in  
441 March. These observed ozone structures and their temporal variations are consistently reproduced from GEMS v3.0 retrievals  
442 (Fig. 12b). Notably, during the absent of ozonesonde measurements in early March, GEMS v3.0 provides valuable  
443 supplementary information, revealing a downward propagation of ozone-rich air from the upper to the lower troposphere over  
444 time. Above the tropopause ( $\sim 10$  km), ozone mixing ratios generally exceed 0.1 ppm. The superimposed potential temperature  
445 profiles remained temporally stable in the stratosphere, reflecting persistent stratification and limited vertical dynamical  
446 activity. However, ozone mixing ratios in the lower stratosphere, particularly below 15 km, exhibited marked variability



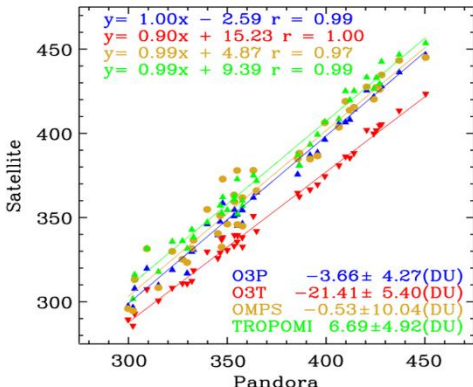
467 between 0.3 and 0.5 ppm, likely associated with isentropic  
 468 transport. GEMS v3.0 effectively captures these variations,  
 469 with enhanced ability to resolve ozone fluctuations in the  
 470 lower stratosphere. However, as shown in Fig 12c, GEMS  
 471 v2.0 produces smoother, less structured patterns.

472 The evaluation of integrated ozone profiles as total  
 473 ozone can provide useful insight into the overall accuracy  
 474 and consistency of vertical profile retrievals when  
 475 compared with well-established ground-based total column  
 476 measurements (Bak et al., 2015). Ground-based Pandora  
 477 total ozone column measurements at Seosan (Park and  
 478 Cede, 2025) are used as a reference to evaluate the total  
 479 ozone integrated from GEMS ozone profiles during the  
 480 Asia-AQ campaign (Figure 13). An intercomparison of  
 481 total ozone columns from GEMS (Baek et al., 2023),  
 482 OMPS (Jaross, 2017), and TROPOMI (Copernicus  
 483 Sentinel-5P, 2020) is also included to assess the  
 484 consistency between GEMS ozone products ( $O_3P$  and  $O_3T$ )  
 485 and to evaluate the relative performance of GEMS  
 486 compared to other satellite observations. As shown, total  
 487 ozone values recorded by Pandora ranged from 300 to 450 DU during February and March 2024. These records closely align  
 488 with satellite observations, evidenced by correlation coefficients of 0.97 or higher across all products. However, the retrievals  
 489 from GEMS  $O_3T$  show inconsistent performance between low  
 490 and high ozone levels, resulting in a regression slope of 0.9,  
 491 whereas the other satellite products exhibit slopes close to  
 492 unity. GEMS  $O_3T$  also significantly underestimates Pandora  
 493 measurements, with a mean bias of  $-20$  DU, primarily due to  
 494 uncertainties in irradiance calibration (Baek et al., 2023). The  
 495 scatter in the OMPS total ozone comparison is larger than that  
 496 of the other products—by a factor of two—likely due to its  
 497 coarse spatial resolution. GEMS  $O_3P$  shows better agreement  
 498 than the other satellite products, both in terms of scatter and

499 **Figure 12. Time series of daily ozone mixing ratio profiles**  
 500 **from ozonesondes and GEMS (v3.0 and v2.0) during the**  
 501 **2024 Asia-AQ campaign. The red line denotes the thermal**  
 502 **tropopause, while the black contour lines (at 50 K**  
 503 **intervals) represent potential temperatures, derived from**  
 504 **the FNL meteorological product.**

479 biases, with mean differences ranging from 1.5 to 8 DU ( $-3.66 \pm 4.27$  DU).

480



481

482 Figure 13. Scatter plots of total ozone columns from GEMS O<sub>3</sub>P, GEMS O<sub>3</sub>T, OMPS, and TROPOMI against Pandora  
483 measurements at Seosan during February–March 2024. A total of 44 Pandora observation days was available, of which 42  
484 remained after quality control. Regression lines and correlation coefficients (r) are shown in the top legend, and mean bias ±  
485  $1\sigma$  in the bottom legend. For comparison, Pandora observations are averaged within  $\pm 30$  min of 04:45 UTC each day and  
486 satellite-Pandora pairs were selected based on the nearest satellite pixel within 100 km

487

488

## 489 5. Conclusions for Version 3 and Remarks for the Next Version

490

491 This study provides the first detailed description of the GEMS operational ozone profile retrieval algorithm in the  
492 literature, along with an analysis of its retrieval characteristics in the 310–330 nm spectral range. The vertical sensitivity of the  
493 GEMS ozone profile is close to unity throughout most of the atmosphere. A decrease to values below 0.5 is observed only in  
494 the lowest five km. Outside of the lower stratosphere (about 15–30 km), the vertical sensitivity is mostly found off-diagonal,  
495 resulting in a rather low average retrieval DFS of about 1.5, up to 3 at maximum. The effective vertical resolution of the GEMS  
496 O<sub>3</sub>P retrieval amounts to 5–10 km.

497 This work primarily highlights substantial algorithmic and calibration enhancements implemented in version 3.0 over  
498 the previous version. Unlike other Level 2 algorithms that typically assume a uniform spectral shift, this work accounts for  
499 independent spectral shifts in radiance and irradiance. To address significant irradiance offsets—arising spatially and  
500 seasonally from BTDF-induced effects, and temporally from optical component degradation—a scaling factor correction is  
501 introduced. This scaling factor basically represents the ratio between the measured irradiance and the solar reference, capturing  
502 systematic deviations due to calibration limitations. Additionally, a soft calibration is applied to compensate for residual  
503 wavelength-dependent uncertainties not addressed by the scaling factor, as well as for spatial (cross-track) variations in

504 normalized radiance. The GEMS soft spectra are derived from clear-sky observations during the week of July 11–17, 2021,  
505 at 02:45 UTC, to address systematic residuals between measured and simulated normalized radiances as a function of spatial  
506 pixel, and are applied uniformly across all observation times. We also adopt the newly implemented forward model, additional  
507 fitting parameters, and auxiliary data from the OMI Collection 4 ozone profile algorithm (Bak et al., 2024). As a result, version  
508 3.0 achieves a spectral fitting residual of 0.2% (low SZA/VZA) in ozone profile retrievals, indicating a fourfold improvement  
509 compared to version 2.0. Validation results further confirm the improved performance of the version 3.0 ozone profile product.  
510 Comparisons with regular ozonesonde observations from six East and Southeast Asian stations reveal substantial bias reduction  
511 and improved consistency in both the troposphere and lower stratosphere, effectively smoothing the altitude-dependent  
512 oscillating biases observed in version 2.0. The mean tropospheric ozone column bias is reduced from +36.2% in version 2.0  
513 to −7.7% in version 3.0, accompanied by an improvement in the correlation coefficient from 0.80 to 0.87. Stratospheric  
514 retrievals also show good agreement, with a mean bias of 4.3% and a correlation coefficient of 0.92. Time series comparisons  
515 of tropospheric ozone demonstrate a better representation of the seasonal cycle in version 3.0, whereas version 2.0 exhibited  
516 an artificial increasing trend. Additional validation using ozonesonde data from the 2024 Asia-AQ campaign supports the  
517 improved vertical structure and day-to-day variability captured by GEMS version 3.0. Furthermore, GEMS total ozone  
518 columns derived from version 3.0 profiles show excellent agreement with Pandora measurements ( $r = 0.99$ , mean bias = −3.7  
519 DU), outperforming the GEMS total ozone product. The reprocessing of the GEMS ozone profile dataset has been completed  
520 and the version 3 product is publicly available through the Environmental Satellite Center website  
521 (<https://nesc.nier.go.kr/en/html/datasvc/index.do>; NIER, 2025).

522 In this study, we focused on the afternoon measurements at 04:45 UTC (13:45 local time, KST), which correspond to  
523 the overpass time of polar-orbiting satellites in East Asia. In the next version (version 4), we will aim to improve and validate  
524 the ozone profile product for hourly observations. Irradiance calibration will be enhanced by accounting for BTDF effects and  
525 optical degradation in the Level 1C processing, which is expected to provide a more robust foundation for both ozone profile  
526 retrievals and auxiliary input data such as total ozone and cloud information. In turn, the use of soft spectra will be extended  
527 to support hourly, seasonal, and yearly applications, enabling improved temporal consistency in the quality of the GEMS ozone  
528 profile product for both diurnal variation analysis and long-term atmospheric monitoring.

## 529 Acknowledgements

530 We thank the GEMS science team and the Environmental Satellite Center (ESC) of the National Institute of Environmental  
531 Research (NIER) for their support in the development of the GEMS ozone profile retrieval algorithm. We also acknowledge  
532 the contributions of the TEMPO, ESA PEGASUS, and ASIA-AQ, WOUDC, SHADOZ teams to algorithm improvements and  
533 product validation.

534 **Competing interests.** The authors have no competing interests

536

537 **Code availability**

538 The GEMS L2 O<sub>3</sub>P algorithm is not available publicly.

539 **Data availability**

540 GEMS L2 O<sub>3</sub>P data can be obtained from the Environmental Satellite Center website  
541 (<https://nesc.nier.go.kr/en/html/datasvc/index.do>; NIER, 2025) (current version is 3.0 for entire mission). The Asia-AQ  
542 campaign archives are available from <https://www-air.larc.nasa.gov/missions/asia-aq/> (NASA, 2023). The regular ozonesonde  
543 observations are downloaded from the WOUDC, SHADOZ, and KMA websites.

544

545 **Financial support**

546 This research was supported by Basic Science Research Program through the National Research Foundation of Korea  
547 (NRF) funded by the Ministry of Education (grant no. 2020R1A6A1A03044834 and 2021R1A2C1004984). Additional  
548 support was provided by a grant from the National Institute of Environment Research (NIER), funded by the Ministry of  
549 Environment (MOE) of the Republic of Korea (grant no. NIER-2025-04-02-063). GEMS O<sub>3</sub>P retrieval characterization and  
550 validation studies were performed within the PEGASOS (Product Evaluation of GEMS L2 via Assessment with S5P and Other  
551 Sensors) project funded by the European Space Agency (ESA) (contract No. 4000138176/22/I-DT-lr). X.L. and G.G.A were  
552 supported by the NASA TEMPO project (Contract No. NNL13AA09C) as well as the NASA Grant 80NSSC19K1626.

553

554 **Author Contributions** J.B., D.C., J.K. (Jae-Hwan Kim), X.L., and K.Y. developed the ozone profile retrieval algorithm.  
555 G.G.A. developed the radiance data reading modules. A.K. and J.C.L. performed the retrieval characterization. J.H.K. (Ja-Ho  
556 Koo) and J.K. (Joowan Kim) provided the Asia-AQ ozonesonde data. S.H., K.B., Y.J and K.P.H. conducted the validation.  
557 C.H.K., H.L., and W.J. advised on the implementation of meteorological reanalysis and forecast data. J.K. (Jhoon Kim) led  
558 the overall GEMS project. H.H. and W.L. managed the project. All authors contributed to the data analysis and manuscript  
559 preparation.

560

561 **References**

562

563 Baek, K., Kim, J. H., Bak, J., Haffner, D. P., Kang, M. and Hong, H.: Evaluation of total ozone measurements from  
564 Geostationary Environmental Monitoring Spectrometer (GEMS), *Atmos. Meas. Tech.*, 16(22), 5461–5478,  
565 doi:10.5194/amt-16-5461-2023, 2023.

566 Baek, K., Bak, J., Kim, J. H., Park, S. S., Haffner, D. P. and Lee, W.: Validation of geostationary environment monitoring  
567 spectrometer (GEMS), TROPOspheric Monitoring Instrument (TROPOMI), and Ozone Mapping and Profiler Suite

- 568 Nadir Mapper (OMPS) using pandora measurements during GEMS Map of Air Pollution (GMAP) field campaig,  
569 Atmos. Environ., 324(August 2023), 120408, doi:10.1016/j.atmosenv.2024.120408, 2024.
- 570 Bak, J., Liu, X., Wei, J. C., Pan, L. L., Chance, K. and Kim, J. H.: Improvement of omi ozone profile retrievals in the upper  
571 troposphere and lower stratosphere by the use of a tropopause-based ozone profile climatology, Atmos. Meas. Tech.,  
572 6(9), 2239–2254, doi:10.5194/amt-6-2239-2013, 2013.
- 573 Bak, J., Liu, X., Kim, J. H., Chance, K. and Haffner, D. P.: Validation of OMI total ozone retrievals from the SAO ozone  
574 profile algorithm and three operational algorithms with Brewer measurements, Atmos. Chem. Phys., 15(2), 667–683,  
575 doi:10.5194/acp-15-667-2015, 2015.
- 576 Bak, J., Liu, X., Kim, J.-H., Haffner, D. P., Chance, K., Yang, K. and Sun, K.: Characterization and correction of OMPS nadir  
577 mapper measurements for ozone profile retrievals, Atmos. Meas. Tech., 10(11), 4373–4388, doi:10.5194/amt-10-4373-  
578 2017, 2017.
- 579 Bak, J., Kim, J. H., Nam, H., Baek, K. and Shin, D.: Geostationary Environment Monitoring Spectrometer (GEMS) Algorithm  
580 Theoretical Basis Document Ozone Profile Retrieval Algorithm, , (April), 10–11 [online] Available from:  
581 <https://nesc.nier.go.kr/ko/html/satellite/doc/doc.do>, 2020.
- 582 Bak, J., Liu, X., Spurr, R., Yang, K., Nowlan, C. R., Miller, C. C., Abad, G. G. and Chance, K.: Radiative transfer acceleration  
583 based on the principal component analysis and lookup table of corrections: optimization and application to UV ozone  
584 profile retrievals, Atmos. Meas. Tech., 14(4), 2659–2672, doi:10.5194/amt-14-2659-2021, 2021.
- 585 Bak, J., Song, E.-J., Lee, H.-J., Liu, X., Koo, J.-H., Kim, J., Jeon, W., Kim, J.-H. and Kim, C.-H.: Temporal variability of  
586 tropospheric ozone and ozone profiles in the Korean Peninsula during the East Asian summer monsoon: insights from  
587 multiple measurements and reanalysis datasets, Atmos. Chem. Phys., 22(21), 14177–14187, doi:10.5194/acp-22-  
588 14177-2022, 2022.
- 589 Bak, J., Liu, X., Yang, K., Gonzalez Abad, G., O’Sullivan, E., Chance, K. and Kim, C.-H.: An improved OMI ozone profile  
590 research product version 2.0 with collection 4 L1b data and algorithm updates, Atmos. Meas. Tech., 17(7), 1891–1911,  
591 doi:10.5194/amt-17-1891-2024, 2024.
- 592 Bak, J., Liu, X., Abad, G. G. and Yang, K.: An Extension of Ozone Profile Retrievals from TROPOMI Based on the SAO2024  
593 Algorithm, Remote Sens., 17(5), doi:10.3390/rs17050779, 2025a.
- 594 Birk, M. and Wagner, G.: ESA SEOM-IAS – Measurement and ACS database O3 UV region, ,  
595 doi:10.5281/ZENODO.1485588, 2018.
- 596 Brion, J., Chakir, A., Daumont, D., Malicet, J. and Parisse, C.: High-resolution laboratory absorption cross section of O3.  
597 Temperature effect, Chem. Phys. Lett., 213(5), 610–612, doi:[https://doi.org/10.1016/0009-2614\(93\)89169-I](https://doi.org/10.1016/0009-2614(93)89169-I), 1993.
- 598 Cai, Z., Liu, Y., Liu, X., Chance, K., Nowlan, C. R., Lang, R., Munro, R. and Suleiman, R.: Characterization and correction of  
599 global ozone monitoring experiment 2 ultraviolet measurements and application to ozone profile retrievals, J. Geophys.  
600 Res. Atmos., 117(7), 1–16, doi:10.1029/2011JD017096, 2012.

- 601 Chance, K. and Kurucz, R. L.: An improved high-resolution solar reference spectrum for earth's atmosphere measurements in  
602 the ultraviolet, visible, and near infrared, *J. Quant. Spectrosc. Radiat. Transf.*, 111(9), 1289–1295,  
603 doi:10.1016/j.jqsrt.2010.01.036, 2010.
- 604 Coddington, O. M., Richard, E. C., Harber, D., Pilewskie, P., Woods, T. N., Chance, K., Liu, X. and Sun, K.: The TSIS-1  
605 Hybrid Solar Reference Spectrum, *Geophys. Res. Lett.*, 1–10, doi:10.1029/2020gl091709, 2021.
- 606 Daumont, D., Brion, J., Charbonnier, J. and Malicet, J.: Ozone UV spectroscopy I: Absorption cross-sections at room  
607 temperature, *J. Atmos. Chem.*, 15(2), 145–155, doi:10.1007/BF00053756, 1992.
- 608 Van Dingenen, R., Dentener, F. J., Raes, F., Krol, M. C., Emberson, L. and Cofala, J.: The global impact of ozone on  
609 agricultural crop yields under current and future air quality legislation, *Atmos. Environ.*, 43(3), 604–618,  
610 doi:<https://doi.org/10.1016/j.atmosenv.2008.10.033>, 2009.
- 611 Dobber, M., Voors, R., Dirksen, R., Kleipool, Q. and Levelt, P.: The high-resolution solar reference spectrum between 250  
612 and 550 nm and its application to measurements with the ozone monitoring instrument, *Sol. Phys.*, 249(2), 281–291,  
613 doi:10.1007/s11207-008-9187-7, 2008.
- 614 Garane, K., Koukouli, M.-E., Verhoelst, T., Lerot, C., Heue, K.-P., Fioletov, V., Balis, D., Bais, A., Bazureau, A., Dehn, A.,  
615 Goutail, F., Granville, J., Griffin, D., Hubert, D., Keppens, A., Lambert, J.-C., Loyola, D., McLinden, C., Pazmino, A.,  
616 Pommereau, J.-P., Redondas, A., Romahn, F., Valks, P., Van Roozendael, M., Xu, J., Zehner, C., Zerefos, C. and  
617 Zimmer, W.: TROPOMI/S5P total ozone column data: global ground-based validation and consistency with other  
618 satellite missions, *Atmos. Meas. Tech.*, 12(10), 5263–5287, doi:10.5194/amt-12-5263-2019, 2019.
- 619 Hayashida, S., Liu, X., Ono, A., Yang, K. and Chance, K.: Observation of ozone enhancement in the lower troposphere over  
620 East Asia from a space-borne ultraviolet spectrometer, *Atmos. Chem. Phys.*, 15(17), 9865–9881, doi:10.5194/acp-15-  
621 9865-2015, 2015.
- 622 Isaksen, I. S. A., Granier, C., Myhre, G., Berntsen, T. K., Dalsøren, S. B., Gauss, M., Klimont, Z., Benestad, R., Bousquet, P.,  
623 Collins, W., Cox, T., Eyring, V., Fowler, D., Fuzzi, S., Jöckel, P., Laj, P., Lohmann, U., Maione, M., Monks, P.,  
624 Prevot, A. S. H., Raes, F., Richter, A., Rognerud, B., Schulz, M., Shindell, D., Stevenson, D. S., Storelvmo, T., Wang,  
625 W.-C., van Weele, M., Wild, M. and Wuebbles, D.: Atmospheric composition change: Climate–Chemistry interactions,  
626 *Atmos. Environ.*, 43(33), 5138–5192, doi:<https://doi.org/10.1016/j.atmosenv.2009.08.003>, 2009.
- 627 Kang, M., Ahn, M. H., Ko, D. H., Kim, J., Nicks, D., Eo, M., Lee, Y., Moon, K. J. and Lee, D. W.: Characteristics of the  
628 Spectral Response Function of Geostationary Environment Monitoring Spectrometer Analyzed by Ground and In-Orbit  
629 Measurements, *IEEE Trans. Geosci. Remote Sens.*, 60, 1–16, doi:10.1109/TGRS.2021.3091677, 2022.
- 630 Kang, M., Ahn, M.-H., Lee, Y., Ho Ko, D., Eo, M., Kim, J. and Moon, K.-J.: On-Orbit Correction of Bi-Directional  
631 Transmittance Distribution Function (BTDF) of Geostationary Environment Monitoring Spectrometer (GEMS), *IEEE*  
632 *Trans. Geosci. Remote Sens.*, 62, 1–15, doi:10.1109/TGRS.2024.3510337, 2024.
- 633 Keppens, A., Lambert, J.-C., Granville, J., Miles, G., Siddans, R., van Peet, J. C. A., van der A, R. J., Hubert, D., Verhoelst,  
634 T., Delcloo, A., Godin-Beekmann, S., Kivi, R., Stübi, R. and Zehner, C.: Round-robin evaluation of nadir ozone profile

- 635 retrievals: methodology and application to MetOp-A GOME-2, *Atmos. Meas. Tech.*, 8(5), 2093–2120,  
636 doi:10.5194/amt-8-2093-2015, 2015.
- 637 Kim, J., Jeong, U., Ahn, M.-H., Kim, J. H., Park, R. J., Lee, H., Song, C. H., Choi, Y.-S., Lee, K.-H., Yoo, J.-M., Jeong, M.-J.,  
638 Park, S. K., Lee, K.-M., Song, C.-K., Kim, S.-W., Kim, Y. J., Kim, S.-W., Kim, M., Go, S., Liu, X., Chance, K., Miller,  
639 C. C., Al-Saadi, J., Veihelmann, B., Bhartia, P. K., Torres, O., Abad, G. G., Haffner, D. P., Ko, D. H., Lee, S. H., Woo,  
640 J.-H., Chong, H., Park, S. S., Nicks, D., Choi, W. J., Moon, K.-J., Cho, A., Yoon, J., Kim, S., Hong, H., Lee, K., Lee,  
641 H., Lee, S., Choi, M., Veefkind, P., Levelt, P. F., Edwards, D. P., Kang, M., Eo, M., Bak, J., Baek, K., Kwon, H.-A.,  
642 Yang, J., Park, J., Han, K. M., Kim, B.-R., Shin, H.-W., Choi, H., Lee, E., Chong, J., Cha, Y., Koo, J.-H., Irie, H.,  
643 Hayashida, S., Kasai, Y., Kanaya, Y., Liu, C., Lin, J., Crawford, J. H., Carmichael, G. R., Newchurch, M. J., Lefer, B.  
644 L., Herman, J. R., Swap, R. J., Lau, A. K. H., Kurosu, T. P., Jaross, G., Ahlers, B., Dobber, M., McElroy, C. T. and  
645 Choi, Y.: New Era of Air Quality Monitoring from Space: Geostationary Environment Monitoring Spectrometer  
646 (GEMS), *Bull. Am. Meteorol. Soc.*, 101(1), E1–E22, doi:10.1175/BAMS-D-18-0013.1, 2020.
- 647 Kim, J. H., Baek, K. and Lee, H.: Geostationary Environment Monitoring Spectrometer (GEMS) Algorithm Theoretical Basis  
648 Document Total Column Ozone Retrieval Algorithm, , (December) [online] Available from:  
649 <https://nesc.nier.go.kr/ko/html/satellite/doc/doc.do>, 2024.
- 650 Kuang, S., Newchurch, M. J., Johnson, M. S., Wang, L., Burris, J., Pierce, R. B., Eloranta, E. W., Pollack, I. B., Graus, M., de  
651 Gouw, J., Warneke, C., Ryerson, T. B., Markovic, M. Z., Holloway, J. S., Pour-Bazar, A., Huang, G., Liu, X. and  
652 Feng, N.: Summertime tropospheric ozone enhancement associated with a cold front passage due to stratosphere-to-  
653 troposphere transport and biomass burning: Simultaneous ground-based lidar and airborne measurements, *J. Geophys.  
654 Res. Atmos.*, 122(2), 1293–1311, doi:<https://doi.org/10.1002/2016JD026078>, 2017.
- 655 Lee, K., Lee, D.-W., Chang, L.-S., Yu, J.-A., Lee, W.-J., Kang, K.-H. and Jeong, J.: Pioneering Air Quality Monitoring over  
656 East and Southeast Asia with the Geostationary Environment Monitoring Spectrometer (GEMS), *Korean J. Remote  
657 Sens.*, 40(5), 741–752, doi:10.7780/kjrs.2024.40.5.2.5, 2024.
- 658 Liu, X., Chance, K., Sioris, C. E., Spurr, R. J. D., Kurosu, T. P., Martin, R. V. and Newchurch, M. J.: Ozone profile and  
659 tropospheric ozone retrievals from the Global Ozone Monitoring Experiment: Algorithm description and validation, *J.  
660 Geophys. Res.*, 110(D20), D20307, doi:10.1029/2005JD006240, 2005.
- 661 Liu, X., Bhartia, P. K., Chance, K., Spurr, R. J. D. and Kurosu, T. P.: Ozone profile retrievals from the Ozone Monitoring  
662 Instrument, *Atmos. Chem. Phys.*, 10(5), 2521–2537, doi:10.5194/acp-10-2521-2010, 2010.
- 663 Lu, X., Zhang, L., Liu, X., Gao, M., Zhao, Y. and Shao, J.: Lower tropospheric ozone over India and its linkage to the South  
664 Asian monsoon, *Atmos. Chem. Phys.*, 18(5), 3101–3118, doi:10.5194/acp-18-3101-2018, 2018.
- 665 Malicet, J., Daumont, D., Charbonnier, J., Parisse, C., Chakir, A. and Brion, J.: Ozone UV spectroscopy. II. Absorption cross-  
666 sections and temperature dependence, *J. Atmos. Chem.*, 21(3), 263–273, doi:10.1007/BF00696758, 1995.
- 667 McPeters, R. D. and Labow, G. J.: Climatology 2011: An MLS and sonde derived ozone climatology for satellite retrieval  
668 algorithms, *J. Geophys. Res. Atmos.*, 117(D10), doi:<https://doi.org/10.1029/2011JD017006>, 2012.

669 Monks, P. S., Archibald, A. T., Colette, A., Cooper, O., Coyle, M., Derwent, R., Fowler, D., Granier, C., Law, K. S., Mills, G.  
670 E., Stevenson, D. S., Tarasova, O., Thouret, V., von Schneidemesser, E., Sommariva, R., Wild, O. and Williams, M. L.:  
671 Tropospheric ozone and its precursors from the urban to the global scale from air quality to short-lived climate forcer,  
672 Atmos. Chem. Phys., 15(15), 8889–8973, doi:10.5194/acp-15-8889-2015, 2015.  
673 Rodgers, C. D.: Inverse Methods for Atmospheric Sounding, WORLD SCIENTIFIC., 2000.  
674 Solomon, S.: Stratospheric ozone depletion: A review of concepts and history, Rev. Geophys., 37(3), 275–316,  
675 doi:<https://doi.org/10.1029/1999RG900008>, 1999.  
676 Zhao, F., Liu, C., Cai, Z., Liu, X., Bak, J., Kim, J., Hu, Q., Xia, C., Zhang, C., Sun, Y., Wang, W. and Liu, J.: Ozone profile  
677 retrievals from TROPOMI: Implication for the variation of tropospheric ozone during the outbreak of COVID-19 in  
678 China, Sci. Total Environ., 764, 142886, doi:10.1016/j.scitotenv.2020.142886, 2021.  
679  
680  
681 <references which is added manually>  
682 NASA: *Draft Planning Document for ASIA-AQ*, available at:  
683 [https://espo.nasa.gov/sites/default/files/documents/Draft%20Planning%20Document%20for%20ASIA-AQ\\_20230720.pdf](https://espo.nasa.gov/sites/default/files/documents/Draft%20Planning%20Document%20for%20ASIA-AQ_20230720.pdf) (last access: 20 August 2025), 2023.  
684 National Institute of Environmental Research (NIER): GEMS data, Environmental Satellite Center [data set], available at:  
685 <https://nesc.nier.go.kr/en/html/datasvc/index.do> (last access: 20 August 2025).  
686 Livesey, N. J., Read, W. G., Wagner, P. A., Froidevaux, L., Santee, M. L., Schwartz, M. J., Lambert, A., Millán Valle, L. F.,  
687 Pumphrey, H. C., Manney, G. L., et al.: EOS MLS Version 5.0x Level 2 and 3 Data Quality and Description Document,  
688 Tech. Rep., Jet Propulsion Laboratory, D-105336 Rev. B, 30 January 2022, available at: <https://mls.jpl.nasa.gov/eos-aura-mls/documentation.php> (last access: 20 August 2025).  
689 Jaross, G.: OMPS-NPP L2 NM Ozone ( $O_3$ ) Total Column Swath Orbital V2, Goddard Earth Sciences Data and Information  
690 Services Center (GES DISC), Greenbelt, MD, USA, <https://doi.org/10.5067/0WF4HAAZ0VHK>, last access: 20 August  
691 2025.  
692 Copernicus Sentinel-5P (processed by ESA), 2020, TROPOMI Level 2 Ozone Total Column products. Version 02. European  
693 Space Agency. <https://doi.org/10.5270/S5P-ft13p57>, last access: 20 August 2025.  
694 Park, J. and Cede, A.: Pandora total ozone column data at Seosan (P164s1), Institute of Atmospheric Environment, Chungcheong  
695 Province, Republic of Korea, <https://doi.org/10.48956/pgn.rout2p1-8.Seosan.P164s1>, last access: 20 August 2025.  
696 Bak, J., et al.: Geostationary Environment Monitoring Spectrometer (GEMS): Long-Term Radiometric Accuracy and Spectral  
697 Stability from 4.5 years of In-Orbit Solar Irradiance Observations, in review, IEEE Trans. Geosci. Remote Sens., 2025b.  
698  
700 (This paper is currently under review with a minor revision requested. The reference will be updated with the DOI if accepted  
701 and published; otherwise, it will be excluded.)